

1 **Direct observation of core-shell structure and water**
2 **uptake of individual submicron urban aerosol particles**

3 Ruiqi Man¹, Yishu Zhu^{1,†}, Zhijun Wu^{1,2,*}, Peter Aaron Alpert^{3,‡}, Bingbing Wang⁴, Jing
4 Dou^{5,§}, Jie Chen⁵, Yan Zheng¹, Yanli Ge¹, Qi Chen¹, Shiyi Chen¹, Xiangrui Kong⁶,
5 Markus Ammann³, Min Hu¹

6 ¹State Key Joint Laboratory of Environmental Simulation and Pollution Control, College of
7 Environmental Sciences and Engineering, Peking University, Beijing, 100871, China

8 ²Collaborative Innovation Center of Atmospheric Environment and Equipment Technology, Nanjing
9 University of Information Science and Technology, Nanjing, 210044, China

10 ³Laboratory of Atmospheric Chemistry, PSI Center for Energy and Environmental Sciences, Paul
11 Scherrer Institute, Villigen, 5234, Switzerland

12 ⁴College of Ocean and Earth Sciences, State Key Laboratory of Marine Environmental Science,
13 Xiamen University, Xiamen, 361102, China

14 ⁵Institute for Atmospheric and Climate Science, ETH Zürich, Zürich, 8092, Switzerland

15 ⁶Department of Chemistry and Molecular Biology, University of Gothenburg, Gothenburg, 41390,
16 Sweden

17 [†]now at Department of Earth and Planetary Science, University of California Berkeley, Berkeley, CA,
18 94720, USA

19 [‡]now at XRnanotech GmbH, Parkstrasse 1, Villigen, 5234, Switzerland

20 [§]now at Institute for Atmospheric and Earth System Research, University of Helsinki, Helsinki, 00014,
21 Finland

22 **Correspondence to:* Zhijun Wu (zhijunwu@pku.edu.cn)

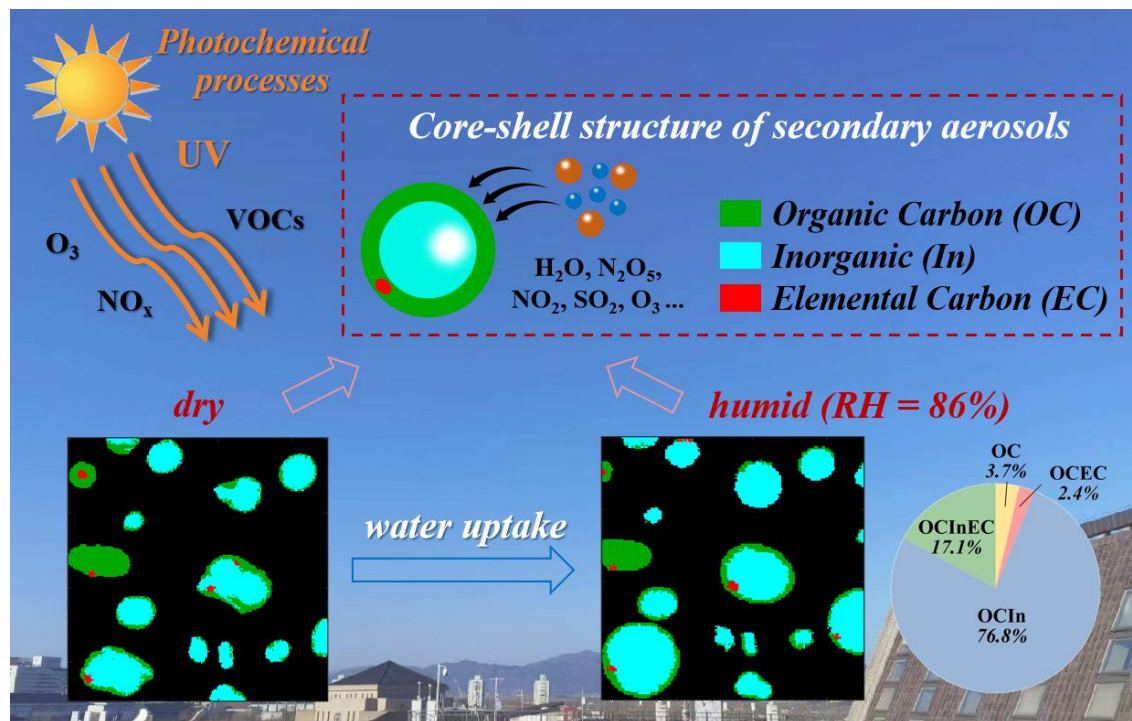
23 **Abstract.** Determining the particle chemical morphology is crucial for unraveling reactive uptake in
24 atmospheric multiphase and heterogeneous chemistry. However, it remains challenging due to the
25 complexity and inhomogeneity of aerosols particles. Using a scanning transmission X-ray microscopy
26 (STXM) coupled with near-edge X-ray absorption fine structure (NEXAFS) spectroscopy and an
27 environmental cell, we imaged and quantified the chemical morphology and hygroscopic behavior of
28 individual submicron urban aerosol particles. Results show that internally mixed particles composed of
29 organic carbon and inorganic matter (OCIn) dominated the particle population ($73.1 \pm 7.4\%$). At 86%
30 relative humidity, 41.6% of the particles took up water, with OCIn particles constituting 76.8% of these
31 hygroscopic particles. Most particles exhibited a core-shell structure under both dry and humid
32 conditions, with an inorganic core and an organic shell. Our findings provide direct observational

33 evidence of the core-shell structure and water uptake behavior of typical urban aerosols, which
34 underscore the importance of incorporating the core-shell structure into models for predicting the
35 reactive uptake coefficient of heterogeneous reactions.

36 **Short summary:** The particle chemical morphology is important to atmospheric multiphase and
37 heterogeneous chemistry. This work directly observed the core-shell structure and water uptake
38 behavior of individual submicron aerosol particles at an urban site and elucidated the potential impact
39 on particle reactive uptake and heterogeneous reactions.

40 **Keywords:** urban air pollution; individual particles; chemical morphology; core-shell structure; water
41 uptake

42 **Table of Contents Graphic:**



43

44 **1 Introduction**

45 Aerosols have significant impacts on visibility, climate, and human health (McCormick and
46 Ludwig, 1967; Noll et al., 1968; Chow et al., 2006; Rasool and Schneider, 1971). As particles in the
47 atmosphere usually act as reaction vessels for various reactions, the physicochemical properties of
48 aerosol particles play an important role in reactive uptake of gaseous molecules onto particles, mass
49 transfer and gas-particle partitioning equilibrium, and transformation mechanisms of pollutants (Abbatt
50 et al., 2012; Davidovits et al., 2011; George et al., 2015; George and Abbatt, 2010; Su et al., 2020;
51 Ziemann and Atkinson, 2012). Therefore, quantitatively characterizing the aerosol physicochemical
52 properties is vital to atmospheric multiphase and heterogeneous chemistry (Freedman, 2017; Li et al.,
53 2016; Riemer et al., 2019; Tang et al., 2016).

54 The aerosol physicochemical properties, such as the particle size, chemical morphology (defined
55 as the spatial distribution of various chemical components within a particle herein), mixing state, and
56 hygroscopicity vary under different ambient conditions. These properties and their variations have a
57 critical influence on reactive uptake, a key process in multiphase chemistry which is initiated by the
58 collision of a gas-phase reactant with a condensed-phase surface (Davies and Wilson, 2018; Reynolds
59 and Wilson, 2025). Organic coatings of particles with core-shell structures inhibit reactive uptake of
60 dinitrogen pentoxide (N_2O_5) by particulate matter by means of affecting mass accommodation, the
61 availability of water for hydrolysis, and mass transport (Wagner et al., 2013; Jahl et al., 2021; Jahn et
62 al., 2021). Without considering the core-shell structure, the reactive uptake coefficient of N_2O_5 tends to
63 be overestimated from several times to tens of times (Wagner et al., 2013). Therefore, investigating the
64 particle chemical morphology is necessary for accurately quantifying the uptake coefficient and
65 reducing uncertainty in heterogeneous reactions.

66 So far, extensive research has been conducted on the physicochemical properties of bulk aerosols
67 by various techniques, such as the Humidified Tandem Differential Mobility Analyzer (H-TDMA),
68 Aerosol Mass Spectrometer (AMS), and Soot Particle Aerosol Mass Spectrometer (SP-AMS) (Li et al.,
69 2016; Tang et al., 2019; Riemer et al., 2019). However, the bulk analysis mostly obtains indirect
70 information about the physicochemical properties of particle populations based on assumptions and
71 estimations, which is difficult to directly observe the chemical morphology and mixing state of aerosol
72 particles (Li et al., 2016). This knowledge gap hinders our understanding of the role of aerosol particles

删除[Ruiqi Man]: particle aerosols

73 in reactive uptake and heterogeneous processes. As a comparison, individual particle analysis can
74 provide direct observational evidence about the chemical morphology and mixing state at the
75 microscopic scale, which is essential for exploring particle hygroscopic and optical properties (Krieger
76 et al., 2012; Li et al., 2016; Posfar et al., 2010; Wu and Ro, 2020).

77 Scanning transmission X-ray microscopy combined with near-edge X-ray absorption fine
78 structure (STXM/NEXAFS) spectroscopy bases on synchrotron radiation technology. It is a robust
79 technique for obtaining chemical morphology information of numerous individual particles with high
80 spectral energy resolution and chemical specificity, as it can identify and distinguish various chemical
81 composition at the single particle level within a particle population (Moffet et al., 2011; Shao et al.,
82 2022). The soft X-ray energy range of STXM (100 - 2000 eV for STXM versus 50 - 200 keV for
83 electron microscopy) makes it possible to quantify light elements (such as carbon, nitrogen, and
84 oxygen) with little beam damage (Moffet et al., 2011). In addition, STXM doesn't require ultrahigh
85 vacuum conditions (Moffet et al., 2011). In short, STXM/NEXAFS spectroscopy provides an enhanced
86 chemical sensitivity for obtaining specific organic chemical bonds, functional groups, and speciation
87 information, which has enormous potential in exploring ambient samples under atmospheric relevant
88 conditions, especially submicron-sized particles.

89 Compared with other STXM endstations which generally analyze samples under vacuum
90 conditions (Alpert et al., 2022; Bondy et al., 2018; Fraund et al., 2020; Knopf et al., 2023; Lata et al.,
91 2021; Moffet et al., 2010a; Moffet et al., 2010b; Moffet et al., 2013; Moffet et al., 2016; Tomlin et al.,
92 2022), several STXM instruments are equipped with an in-situ temperature and relative humidity (RH)
93 control environmental cell, allowing for investigating hygroscopicity and water uptake behavior of
94 laboratory-generated particles (Ghorai and Tivanski, 2010; O'brien et al., 2015; Piens et al., 2016;
95 Zelenay et al., 2011a; Zelenay et al., 2011b). However, only a few researches focusing on hygroscopic
96 behavior of ambient particles has been reported so far, and these particles were collected in rural
97 environment (Piens et al., 2016) or forest (Mikhailov et al., 2015; Pöhlker et al., 2014). Studies on
98 water uptake of urban aerosol particles using STXM and corresponding knowledge for their chemical
99 morphology under humid conditions is currently lacking.

100 In recent years, the air quality in China has improved notably due to the implementation of a
101 series of strict pollution mitigation measures. These improvements are attributed to decreasing primary
102 emissions, while the contributions of secondary species to particle mass have become more significant

刪除[Ruiqi Man]: resolve compositional contrast

刪除[Ruiqi Man]: Compared with electron microscopy
which is not well-suited for analyzing organic species, t

刪除[Ruiqi Man]: C

刪除[Ruiqi Man]: N

刪除[Ruiqi Man]: O

刪除[Ruiqi Man]: high chemical specificity, high spatial
resolution, and

刪除[Ruiqi Man]: ; Shao et al., 2022

刪除[Ruiqi Man]: Therefore, STXM/NEXAFS spectroscopy
has enormous potential in exploring ambient samples under
atmospheric relevant conditions, especially submicron-sized
particles.

103 (Lei et al., 2021; Wang et al., 2019). To elucidate the causes and mechanisms of pollution episodes in
104 China, numerous research has been carried out on the pollution characteristics (Gao et al., 2015; Gao et
105 al., 2018; Guo et al., 2014; Huang et al., 2014; Liu et al., 2018; Sun et al., 2013; Wang et al., 2014;
106 Zhao et al., 2013) and physicochemical properties (Gao and Anderson, 2001; Li et al., 2017; Shen et al.,
107 2019; Song et al., 2022) of ambient aerosols. However, there is still a lack of studies on direct
108 observation of the chemical morphology and hygroscopic behaviors of secondary urban aerosols at the
109 single particle level. This knowledge gap hinders our understanding of the role of secondary aerosols as
110 reaction vessels in heterogeneous reactions.

111 In this study, we investigated the chemical morphology of ambient individual submicron aerosol
112 particles using STXM/NEXAFS spectroscopy. The ambient samples were collected at an urban site in
113 Beijing of North China Plain during a pollution episode. We also explored the chemical morphology
114 and water uptake behavior of individual particles at high humidity (RH = 86%) using an environmental
115 cell. This work aims to improve our comprehension of the physicochemical properties of particles in
116 typical urban pollution atmospheres, aiding in clarifying their atmospheric heterogeneous processes
117 and multiphase chemistry.

删除[Ruiqi Man]: in

118 2 Materials and methods

119 2.1 Sampling and instruments

120 To study the physicochemical properties of ambient particles, samples were collected during a
121 pollution episode at the Peking University Urban Atmosphere Environment Monitoring Station
122 (PKUERS, 39°59'21"N, 116°18'25"E) in Beijing, China. More details about the measurement site can
123 be found in our previous studies (Tang et al., 2021; Wu et al., 2007).

124 The individual particle sample was collected using a four-stage cascade impactor with a Leland
125 Legacy personal sample pump (Sioutas, SKC, Inc., the US) at a flow rate of 9 L min⁻¹. The sampling
126 started at 5:04 P.M. on October 1st, 2019 and lasted for 5 minutes. The sampling substrate was a copper
127 grid (Lacey Carbon 200 mesh, Ted Pella, Inc., the US) suitable for its X-ray transparency. Particles
128 collected onto the last stage with the 50% cut-point aerodynamic diameter of 250-nm were used for
129 STXM analysis. The sample was placed into a sample box sealed with a bag filled with nitrogen, and it
130 was stored in a freezer at a temperature of -18°C until analysis.

131 Other parameters were measured from September 28th to October 7th, 2019. The non-refractory
132 chemical composition of submicron particles (NR-PM₁) was obtained by a Long Time-of-Flight
133 Aerosol Mass Spectrometer (LTOF-AMS, Aerodyne Research Inc., the US) (Zheng et al., 2020; Zheng
134 et al., 2023). Calibrations of ionization efficiency (IE) and relative IE followed the standard procedures
135 described in previous studies (Canagaratna et al., 2007; Fröhlich et al., 2013). The reference
136 temperature and pressure conditions of mass concentrations reported herein were 293.7 K and 101.82
137 KPa. We applied composition-dependent collection efficiency (CDCE) values (0.50 ± 0.01 , mean \pm
138 standard deviation) that were calculated by the methods introduced by Middlebrook et al. (2012) to the
139 AMS data. The mass concentration of fine particles (PM_{2.5}) was measured by a TEOM analyzer
140 (TH-2000Z1, Wuhan Tianhong Environmental Protection Industry Co., Ltd., China). Meteorological
141 parameters including temperature (T), RH, wind speed, and wind direction were monitored by an
142 integrated 5-parameter Weather Station (MSO, Met One Instruments, Inc., the US).

143 **2.2 STXM/NEXAFS analysis**

144 In order to gain the chemical morphology, mixing state, and component information of individual
145 particles, STXM/NEXAFS spectroscopy measurements were carried out at the PolLux beamline
146 (X07DA) of the Swiss Light Source (SLS) at Paul Scherrer Institute (PSI) (Raabe et al., 2008). In brief,
147 X-rays illuminated a Fresnel zone plate focusing the beam to a pixel of $35 \times 35 \text{ nm}^2$. The zone plate has
148 a central stop that acts together with another optic known as an order sorting aperture to eliminate
149 unfocused and higher-order light, ensuring only first-order focused light is transmitted to the sample.
150 Then, X-rays transmitted through the sample are detected. The absorbance of each pixel is
151 characterized by optical density (OD) based on the Beer-Lambert's law as follows,

$$\text{OD} = -\ln (I/I_0) \quad (1)$$

152 where I and I_0 are the intensity of photons transmitted through a sample region and a sample-free
153 region, respectively. Further details including the uncertainty estimation of OD are described in the
154 Supplementary Information (SI).

155 STXM/NEXAFS spectroscopy scans X-ray energies over particles with high spectral energy
156 resolution. When inner shell electrons of atoms absorb X-ray photons, they can transition into
157 unoccupied valence orbitals, resulting in an absorption peak that is used to identify specific bonding
158 characteristics. The amount of absorption depends on the photon energy (E), elemental composition, as

159 well as sample thickness and density (Moffet et al., 2011). We employed two measurement strategies
160 to optimize photon flux to the particles, achieving the best signal-to-noise ratio while minimizing the
161 scan time. The first strategy was a high energy-resolution mode with an X-ray energy resolution $\Delta E =$
162 0.2 eV and a coarse pixel size of around $100 \times 100 \text{ nm}^2$ to measure absorption at small energy steps.
163 The energy resolution is defined as being able to distinguish between two absorption peaks separated
164 by ΔE at the full width at half maximum OD. In this mode, carbon (C), nitrogen (N), and oxygen (O)
165 K-edge spectra of individual particles were measured. The energy offset of C and O spectra were +0.4
166 eV and +1.2 eV respectively, according to the energy calibration procedures using polystyrene spheres
167 and gas-phase carbon dioxide (CO₂). The energy offset of N at the K-edge was not calibrated, however,
168 the obtained spectra of ambient particles appeared identical to ammonium salts in literatures (Ekimova
169 et al., 2017; Latham et al., 2017). Due to the presence of ammonium, which was confirmed in particles
170 using AMS, we applied a calibration factor of +0.1 eV for the N K-edge to match our observed main
171 peak to that of ammonium at 405.7 eV.

172 The second strategy is a high spatial-resolution mode with a pixel size of $35 \times 35 \text{ nm}^2$ and $\Delta E =$
173 0.6 eV, where imaged at four specific energies for the C K-edge, namely, 278.0 eV, 285.4 eV, 288.6
174 eV, and 320.0 eV. Automated analysis followed the methodology of Moffet et al. (2010a) [and Moffet](#)
175 [et al. \(2016\)](#). In brief, absorption at 278.0 eV (OD_{278.0eV}) is regarded as the pre-edge of carbon, which is
176 mainly due to off-resonance absorption by inorganic elements other than carbon. Absorption at 285.4
177 eV (OD_{285.4eV}) is due to the characteristic transition of sp² hybridized carbon (i.e., doubly bonded
178 carbon). Since this peak is abundant for elemental carbon (EC), it can be used to discern soot, because
179 EC is a type of components of soot (Penner and Novakov, 1996). Absorption at 288.5 eV (OD_{288.5eV})
180 comes from carboxylic carbonyl groups, which are common in organic aerosols in atmospheres.
181 Therefore, organic carbon (OC) is identified by this energy. Absorption of the post-edge at 320.0 eV
182 (OD_{320.0eV}) is contributed by carbonaceous and non-carbonaceous atoms (Moffet et al., 2010a).

183 Based on absorption at these four typical energies, we obtain three images by further processing.
184 The difference between OD at the post-edge and OD at the pre-edge (OD_{320.0eV} - OD_{278.0eV}) indicates
185 total carbon. The ratio of OD at the pre-edge to OD at the post-edge (OD_{278.0eV} / OD_{320.0eV}) indicates the
186 relative absorption contribution of inorganic matter (In). Compared with the absorbance contribution of
187 doubly bonded carbon to total carbon (%sp²) in the highly oriented polycrystalline graphite (HOPG,
188 assuming that %sp² = 100%) at 285.4 eV, the spatial distribution of EC/soot in samples can be

189 identified by the procedure of Hopkins et al. (2007). It is assumed that total carbon consists of OC and
190 EC. [The thresholds of these images follow the criteria mentioned in Moffet et al. \(2010a\) and Moffet et](#)
191 [al. \(2016\).](#) These three images described above were then overlaid to create a chemical map of
192 individual particles.

193 **2.3 Criterion of particle water uptake based on the total oxygen absorbance**

194 To determine whether particles took up water, a criterion was established on the basis of the total
195 oxygen absorbance determined at the energy of 525.0 eV (the pre-edge of oxygen) and 550.0 eV (the
196 post-edge of oxygen). Based on the same principle as the total carbon calculation, the difference
197 between OD at the post-edge and pre-edge of oxygen represents the total oxygen absorbance. Due to
198 the fact that each particle is composed of some pixels, the total oxygen absorbance (ΔOD) of an
199 individual particle under dry and humid conditions is calculated as follows,

$$\Delta OD_{dry} = \sum_{i=1}^m \Delta OD_i = \sum_{i=1}^m (OD_{post,i} - OD_{pre,i}) = \sum_{i=1}^m OD_{post,i} - \sum_{i=1}^m OD_{pre,i} \quad (2)$$

$$\Delta OD_{humid} = \sum_{j=1}^n \Delta OD_j = \sum_{j=1}^n (OD_{post,j} - OD_{pre,j}) = \sum_{j=1}^n OD_{post,j} - \sum_{j=1}^n OD_{pre,j} \quad (3)$$

200 where m and n are numbers of pixels that make up an individual particle under dry and humid
201 conditions, i and j are a certain pixel within an individual particle under dry and humid conditions, *post*
202 and *pre* respectively represent the energy at the post-edge (550.0 eV) and that at the pre-edge (525.0 eV)
203 of oxygen. If a particle takes up water, the amount of oxygen atoms within this particle will increase,
204 leading to an amplification in ΔOD . Water uptake may increase particle height and absorption. On the
205 other hand, it possibly causes a particle to spread out, which may reduce particle height and thus
206 absorption. Although a thinner particle that contains more water may result in less absorption at some
207 specific pixels, ΔOD_{humid} will be larger than ΔOD_{dry} due to the fact that more pixels are summed, i.e.,
208 $n > m$. Therefore, comparing the results of Eq. 2 and Eq. 3 will quantify the total oxygen absorbance of
209 a particle under dry and humid conditions, and determine particle water uptake. Specifically, if
210 $\Delta OD_{humid} > \Delta OD_{dry}$, then we assume that the particle has taken up water.

211 **2.4 A novel in-situ environmental cell**

212 To explore the chemical morphology and hygroscopicity of the particles under humid conditions,
213 we adjusted the RH of an in-situ environmental cell with sample placed in it. The environmental cell
214 can also be used for trace gas reactive uptake and photochemical reactions with laboratory-generated
215 particles (Alpert et al., 2019; Alpert et al., 2021). The environmental cell used in this study consists of a
216 removable sample clip that hosts a sealed silicon nitride (SiNit) window and a main body that contains
217 gas supply lines and temperature control. Together, they are mounted in the STXM vacuum chamber.
218 A SiNit window at the back side of the main body is also sealed and ensures X-ray transparency
219 passing through the whole environmental cell assembly. Descriptions of the connections for the gas
220 supply, heating and cooling devices, and temperature measurement can be found in previous studies
221 (Huthwelker et al., 2010; Zelenay et al., 2011a). The detailed methods of collecting the ambient
222 particles by the impactor and measuring them in the environmental cell were shown in the SI.

223 We performed humidity calibration experiments to make sure sufficient heat transfer and a
224 homogeneous water vapor field across the samples. It is important due to the fact that the only way for
225 samples to gain or lose heat and water was through air contact. To study the accuracy of RH in the
226 environmental cell, water uptake and deliquescence of a sodium chloride (NaCl) standard sample was
227 observed. The deliquescence relative humidity (DRH) of pure NaCl crystals obtained from literatures
228 and thermodynamic models is around 75 – 76% at room temperature (Eom et al., 2014; Martin, 2000;
229 Peng et al., 2022). The images of the NaCl sample displayed in Fig. S1 illustrate the morphological
230 changes as RH increased. As shown in Fig. S1, particle morphologies in panels (A) – (C) remained
231 essentially identical before RH reached the DRH of NaCl, although the focus position slightly varied in
232 different panels. When RH was 75.6% (Fig. S1D), particles completely deliquesced and some
233 coalesced. The uncertainty of RH in the environmental cell in this study was determined conservatively
234 to be $\pm 2\%$, in agreement with previous results (Huthwelker et al., 2010). Information about the oxygen
235 K-edge spectra of the NaCl sample at high RH can be found in Fig. S2.

236 **3 Results and discussion**

237 **3.1 Pollution characteristics during the sampling period**

238 Time series of meteorological parameters, mass concentrations of gaseous pollutants, PM_{2.5}, and
239 NR-PM₁ are shown in Fig. 1. During the pollution episode from September 29th to October 3rd, 2019,

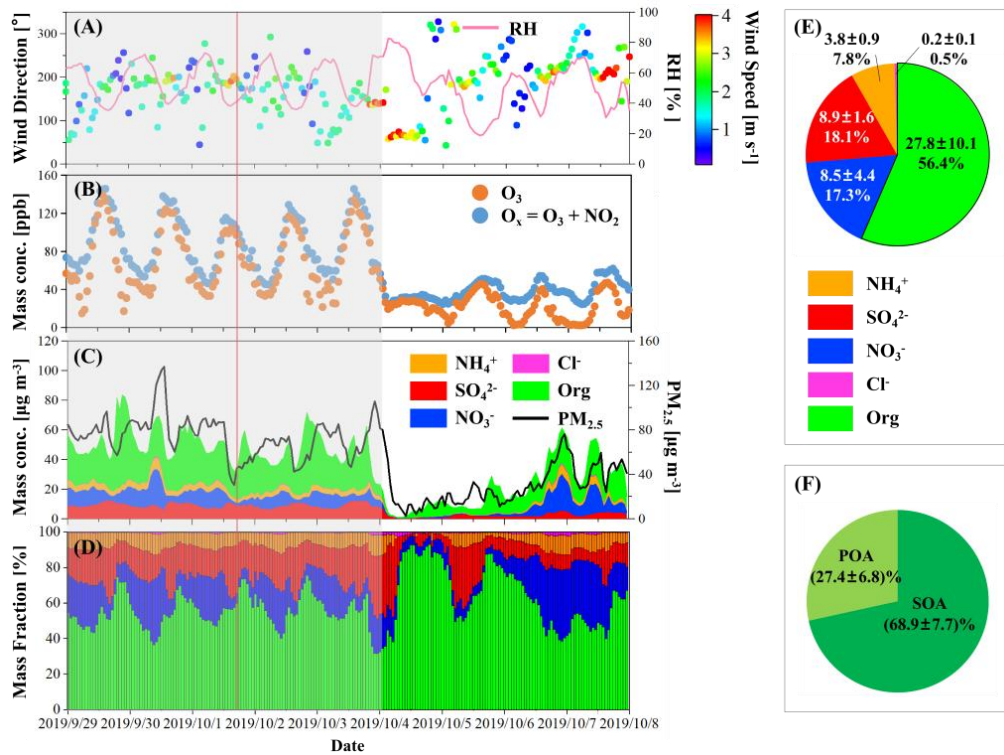
240 the stagnant weather condition with low wind speed led to pollution accumulation. The air became
241 clean due to the appearance of a strong north wind on October 4th (Fig. 1A). The sampling time of the
242 individual particle sample was 5:04 P.M. on October 1st (see the red line in Fig. 1) with an ozone (O₃)
243 concentration of 97.1 ppb. The average mass fractions of chemical composition of NR-PM₁ during the
244 sampling period of individual particles could be found in Fig. S3. During this period, the low mass
245 fraction of volatile inorganic species such as nitrate made it suitable for measurements using offline
246 techniques, such as STXM, because the loss of volatile species during storage and measurement
247 processes was minimal.

248 During the pollution episode, the maximum daily 8-hour average of ozone (MDA8-O₃) was 110.3
249 ± 10.1 ppb (i.e., $236.5 \pm 21.7 \mu\text{g m}^{-3}$). The concentration of O_x [O_x = nitrogen dioxide (NO₂) + O₃] was
250 88.6 ± 29.4 ppb (Fig. 1B), reflecting a high atmospheric oxidation capacity that drives secondary
251 transformations of gaseous pollutants (Dou et al., 2024; Xiao et al., 2022). The average PM_{2.5} was 74.3
252 $\pm 18.3 \mu\text{g m}^{-3}$ (Fig. 1C). As shown in Fig. 1D – 1E, the average mass concentration of secondary
253 inorganic aerosol (SIA) in NR-PM₁ was $21.3 \pm 4.8 \mu\text{g m}^{-3}$, with sulfate and nitrate contributing almost
254 equally to particle mass (i.e., 18.1% and 17.3% respectively). Organic matter in NR-PM₁ had an
255 average mass fraction of 56.4% (Fig. 1E). The mass concentrations of primary organic aerosol (POA)
256 and secondary organic aerosol (SOA) were estimated based on the positive matrix factorization (PMF)
257 analysis (Ulbrich et al., 2009). As shown in Fig. 1F, SOA dominated organic matter, contributing an
258 average of 68.9%. Overall, this pollution episode was led by secondary oxidation processes and
259 featured by high contributions of secondary particulate species.

设置格式[Ruiqi Man]: 下标

删除[Ruiqi Man]: At

删除[Ruiqi Man]: that time



260

261 **Figure 1:** Time series of (A) wind direction, wind speed, and relative humidity (RH), (B) mass
262 concentrations of ozone (O₃) and O_x (O₃ + nitrogen dioxide, NO₂), (C) mass concentrations of fine particles
263 (PM_{2.5}) and non-refractory submicron particles (NR-PM₁), and (D) mass fractions of chemical composition
264 of NR-PM₁ are shown. The gray area represents the pollution episode lasting from September 29th to
265 October 3rd. The red line indicates the sampling time for the individual particle sample. (E) Pie chart
266 showing the average mass fractions of chemical composition of NR-PM₁ during the pollution period. The
267 number in the first row of each part is the average mass concentration and standard deviation (SD) with a
268 unit of µg m⁻³. The number in the second row is the average mass fraction. (F) Pie chart showing the
269 average mass contributions of primary organic aerosol (POA, light green) and secondary organic aerosol
270 (SOA, dark green) to the total organic. Average mass fraction and SD are marked in the pie chart.

271 **3.2 Chemical maps of individual particles**

272 Chemical maps of individual particles under dry conditions are displayed in Fig. 2. Different
273 images denote particles located in different regions of interest (ROI, 12 in total) of the sampling
274 substrate. 197 individual particles were investigated in total. Detailed images of total carbon, inorganic,
275 and doubly bonded carbon maps are available in the SI (Fig. S4 – S6). Most submicron particles on the
276 substrate were round or nearly round, while supermicron particles predominantly exhibited irregular
277 shapes. The circular equivalent diameter of individual particles was calculated, with the methods
278 detailed in the SI. The normalized size distribution of overall particles followed a normal distribution,
279 with a mean diameter ± standard deviation (SD) being 0.83 ± 0.30 µm (Fig. S7A). A significant
280 proportion of the particles were within the 0.4 – 1.2 µm size range.

删除[Ruiqi Man]: 3

删除[Ruiqi Man]: 5

删除[Ruiqi Man]: 6

281 As displayed in Fig. 2, chemical maps of individual particles showed that they were dominated by
282 inorganic substances (colored in cyan), which were likely sulfate that was frequently observed by AMS
283 (Fig. 1C). Approximately one quarter (24.9%) of the particles contained EC/soot (colored in red).
284 Notably, around 82% of these soot-containing particles had soot located at particle edges. One of the
285 possible reasons is that inorganic species (such as crystals) pushed soot away from the center of the
286 particles during their efflorescence (Moffet et al., 2016). Additionally, several particles contained
287 multiple soot components, which was also observed before (Moffet et al., 2016).

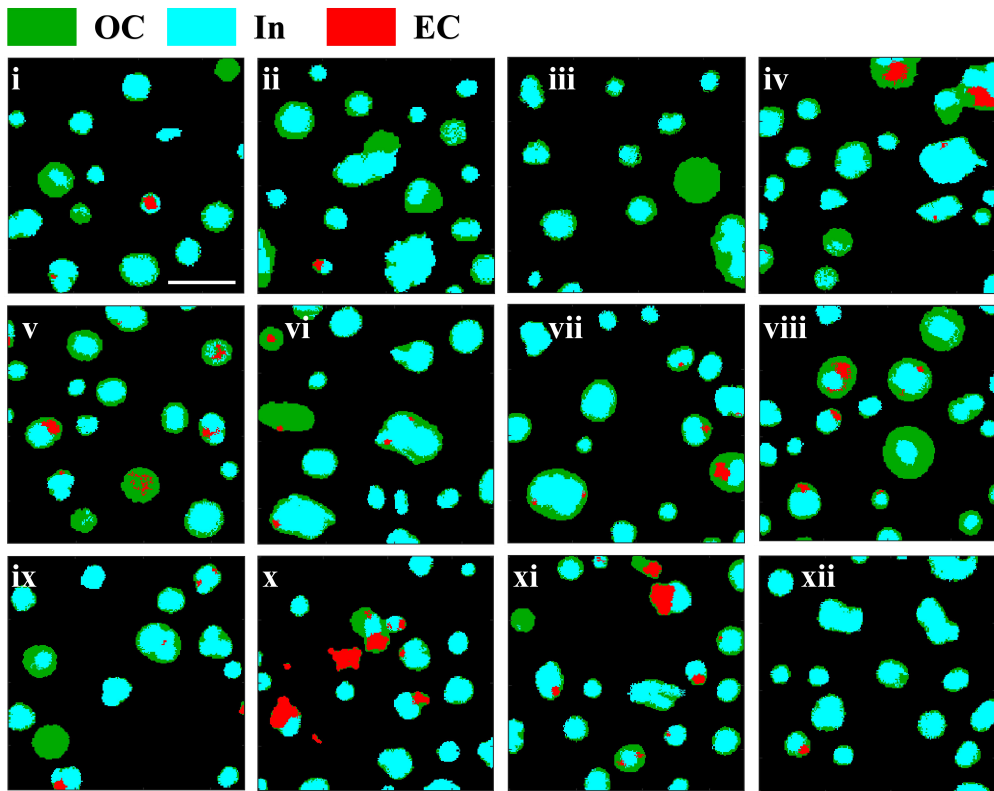
删除[Ruiqi Man]: , found either near the center or at the edge of individual particles

删除[Ruiqi Man]: The

删除[Ruiqi Man]: The morphology of soot varied, showing fractal or compact structures of various sizes.

288 Typically, inorganic components and/or soot were encased in organic matter, forming a core-shell
289 structure characterized by an inorganic-dominated core and an organic-dominated shell. Figure 2
290 illustrates that most organic-inorganic internally mixed particles exhibited thin coatings, likely from
291 fresh emissions. Conversely, a few particles have thick coatings, which is indicative of aging processes
292 in a highly active photochemical environment. Previous studies suggest that most of the
293 soot-containing particles with thin coatings would have rather smaller absorption enhancement
294 compared with those with thick coatings (Bond et al., 2006; Moffet et al., 2016).

295 The observed core-shell morphology could also result from liquid-liquid phase separation (LLPS),
296 influenced by fluctuating ambient RH (Fig. 1A) and determined by the oxygen-to-carbon (O:C) ratio of
297 the organic fraction (Freedman, 2020; Li et al., 2021; You et al., 2012; You et al., 2014; Freedman,
298 2017). To test this hypothesis, the O:C ratio of individual particles composed of pure organic
299 composition was estimated as 0.53 ± 0.15 based on the STXM data. The estimation methods were
300 displayed in the SI. This falls within the threshold range for LLPS occurrence in ammonium sulfate -
301 organic mixing particles ($0 < \text{O:C} < 0.57$) (You et al., 2013).



302

303 **Figure 2: Chemical maps of individual particles in 12 regions of interest (ROI) of sampling substrate under**
 304 **dry conditions on the basis of pixels. Green, cyan, and red color represent dominant components of organic**
 305 **carbon (OC), inorganic matter (In), and elemental carbon (EC), respectively. The scale bar in the upper left**
 306 **image represents 2 μ m and applies to all images.**

307 Statistically, the particles were categorized into four types based on their mixing state, including
 308 pure organic (OC), organic internally mixed with soot (OCEC), organic internally mixed with
 309 inorganic (OCIn), and organic internally mixed with inorganic and soot (OCInEC). OCIn particles
 310 were the most abundant type in the examined particle population ($73.1 \pm 7.4\%$), followed by OCInEC
 311 ($20.8 \pm 6.7\%$) and OCEC ($4.1 \pm 3.3\%$), indicating a highly internally mixed particle population. Pure
 312 organic particles only accounted for $2.0 \pm 2.3\%$. The calculation of the margin of error of the mixing
 313 state proportions can be found in the SI. The mean diameters of OCEC, OCIn, and OCInEC particles
 314 were 0.66, 0.79, and 1.02 μ m, respectively (Fig. S8). This suggests that the internally mixed particles
 315 containing three species families tend to be larger than those composed of two species families.

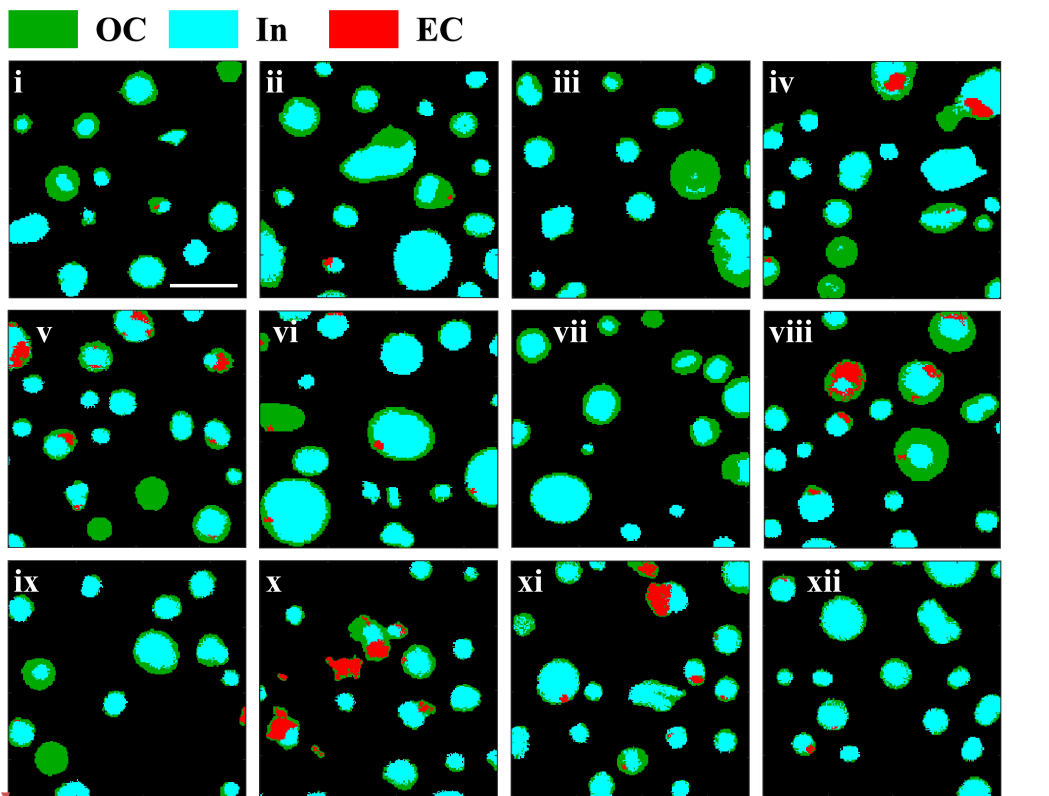
316 **3.3 The effects of particle water uptake on chemical maps**

317 Chemical maps of individual particles under humid conditions (RH = 86%) measured in the
 318 environmental cell were displayed in Fig. 3, and these ROI are identical and matched one by one to

刪除[Ruiqi Man]: 7

319 those in Fig. 2. [For comparison, the one-to-one particle chemical maps of the same region of interest](#)
 320 [under both dry and humid conditions can be found in Fig. S9](#). It was observed that many particles
 321 tended to be more rounded due to water uptake at high RH, especially for particles with diameters in
 322 the supermicron range (e.g., particles in (ii), (vi), (xi), and (xii) in Fig. 3). If particles take up
 323 significant amounts of water and are homogeneously mixed, they would appear as dominated by
 324 inorganic (colored in cyan) due to absorption of a large amount of water at the carbon pre-edge. In
 325 contrast, most particles remained inhomogeneous and exhibited a core-shell structure under humid
 326 conditions. A possible reason is that the settled RH may not reach the mixing relative humidity (MRH)
 327 of particles, which is defined as a threshold where different phases in an aqueous particle mix into one
 328 homogeneous phase. This MRH usually varies from 84% to over 90% (Li et al., 2021; You et al., 2014;
 329 Zhang et al., 2022).

330 Additionally, around 87% of soot was located at the edge of the humidified particles, with no
 331 obvious location change of soot observed in most particles. [A previous study witnessed the](#)
 332 [redistribution of soot within phase-separated particles only after the phase mixing process occurred](#)
 333 [\(Zhang et al., 2022\), which is consistent with the phenomenon observed in our study.](#)



删除[Ruiqi Man]: This phenomenon aligns with a previous study which indicates that the phase transition of phase-separated particles without phase mixing will not cause the redistribution of soot within individual particles (Zhang et al., 2022).

334
 335 **Figure 3: Chemical maps of individual particles in 12 ROI of sampling substrate under humid conditions**
 336 **(RH = 86%) measured in an in-situ environmental cell. Green, cyan, and red color represent dominant**

337 components of OC, In, and EC, respectively. The scale bar in the upper left image represents 2 μm and
338 applied to all images.

339 Comparing size distributions of particle populations under dry (Fig. S7A) and humid conditions
340 (Fig. S7B) reveals that they exhibited similar distribution characteristics. The mean diameter of overall
341 particles at high RH was $0.86 \pm 0.33 \mu\text{m}$, compared with $0.83 \pm 0.30 \mu\text{m}$ under dry conditions. This
342 indicates that the overall size distribution of the humidified particles shifted a little towards larger
343 particles due to water uptake. Specifically, approximately 56.3% of the particles showed an average
344 increase of 14.9% in diameter, while the remaining exhibited an average decrease of 8.2%. Pöhlker et
345 al. (2014) also observed this abnormal phenomenon where some particles decreased in size with
346 increasing RH. They suggested that it could be attributed to the decreasing viscosity and increasing
347 surface tension due to particle water uptake at high RH. This led to larger contact angles between the
348 collected particles and the substrate, causing the particles to 'bead up' and therefore reducing their
349 cross-section areas in the view (Pöhlker et al., 2014). In addition, one should note that a small number
350 of particles at the edge of the ROI did not entirely enter the field of view due to the limited observation
351 range, which may slightly affect the quantification of their size.

352 According to the criterion for water uptake by individual particles based on the total oxygen
353 absorbance described in the Sect. 2.3, 41.6% of the particles took up water. As shown in Fig. S10A,

354 OCIn particles were the dominant mixing state type taking up water (76.8%), followed by OCInEC
355 (17.1%). There were also several OCEC (2.4%) and OC (3.7%) particles displayed water uptake.
356 Different particle mixing state types exhibited distinct patterns of hygroscopic behavior. For instance,
357 43.8% of OCIn particles took up water, while 34.1% of OCInEC particles performed the same. This
358 difference may be attributed to the varying hygroscopicity of different components. For example, the
359 single hygroscopic parameter (κ) of ammonium nitrate, ammonium sulfate, ammonium hydrogen
360 sulfate, POA, and SOA is 0.58, 0.48, 0.56, 0, and 0.1, respectively (Wu et al., 2016). Based on the
361 AMS data, κ of bulk aerosols during the sampling period (0.25 ± 0.01) was calculated according to
362 [κ-Köhler theory](#) (Stokes and Robinson, 1966; Petters and Kreidenweis, 2007), indicating a relatively

363 low hygroscopic capacity of NR-PM₁ during sampling, which could explain why only less than half of
364 the particles exhibited water uptake at such high humidity conditions. In addition, the average diameter
365 of particles taking up water increased from $0.82 \pm 0.33 \mu\text{m}$ to $0.91 \pm 0.36 \mu\text{m}$. The relative frequency
366 distribution and the size-resolved fraction of particles taking up water can be found in Fig. S10B.

删除[Ruiqi Man]: 6

删除[Ruiqi Man]: 6

删除[Ruiqi Man]: 8

删除[Ruiqi Man]: the Zdanovskii-Stokes-Robinson (ZSR)
mixing rule

删除[Ruiqi Man]: 8

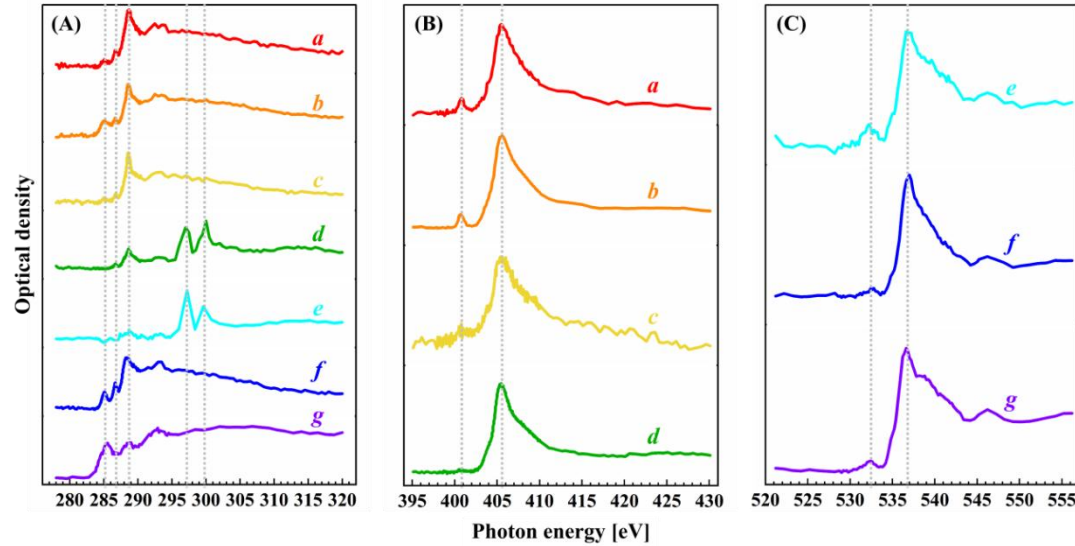
367 **3.4 Chemical composition of ambient submicron particles**

368 NEXAFS spectra with high energy resolution were measured at the C (278 – 320 eV), N (395 –
369 430 eV), and O (525 – 550 eV) K-edges. As shown in Fig. 4A, three notable absorption peaks at the C
370 K-edge were observed at 285.4, 286.7, and 288.6 eV. According to previous literatures (Warwick et al.,
371 1998; Moffet et al., 2010a), the peak at 285.4 eV refers to the characteristic transition of sp^2 hybridized
372 carbon ($C\ 1s \rightarrow \pi^*_{R(C^*=C)R}$). The peak at 286.7 eV may result from the transition of ketonic carbonyl (C
373 $1s \rightarrow \pi^*_{R(C^*=O)R}$), representing ketone and ketone-like compounds. The peak appearing at 288.6 eV
374 represents the characteristic transition of carboxylic carbonyl functional groups ($C\ 1s \rightarrow \pi^*_{R(C^*=O)OH}$),
375 which refers to organic matter and is always found in the outer shell of particles (Moffet et al., 2016;
376 Prather et al., 2013). In addition, two other peaks at 296.8 and 299.6 eV were present (see spectra (d)
377 and (e) in Fig. 4A), corresponding to the L_2 - and L_3 -edges of potassium (K) (Moffet et al., 2010a). In
378 our sample, K may come from biomass burning processes based on a previous study (Wu et al., 2017).

379 Nitrogen K-edge spectra in Fig. 4B illustrate that ammonium salts were the main nitrogen species
380 in the sample. We observed a broad main peak centered at 405.7 eV, which is the feature of ammonium
381 (Ekimova et al., 2017). A smaller peak was observed at 401.0 eV, which is absorption due to nitrogen
382 gas (N_2) either trapped in the inorganic crystal or formed under X-ray exposure (Latham et al., 2017).
383 Absorption of nitrate (NO_3^-) and nitrite (NO_2^-) commonly have narrow peaks at 405.1 eV and 401.7 eV
384 (Smith et al., 2015), respectively, which were not apparent in our spectra. This is likely because
385 particulate nitrite is below the detection limit, or its peak is masked by the pronounced absorption of
386 ammonium (NH_4^+). The solid ammonium nitrate and sodium nitrate salts could exhibit a peak at around
387 415.0 eV (Smith et al., 2015). However, this was not observed in Fig. 4B. Organic compounds
388 containing nitrogen, such as amino acids, N-heterocyclics, and nitroaromatic compounds, can be
389 abundant in urban aerosol particles due to combustion sources (Yu et al., 2024). They have a large
390 variety of possible peak positions, heights, and widths (Leinweber et al., 2007), making the
391 identification of these compounds difficult. Although a positive identification of specific organic
392 nitrides cannot be made, we note that amino acids and 5- or 6-ring heterocycles commonly have narrow
393 peaks at around 401 eV and broad peaks at 405 eV (Leinweber et al., 2007). We expect that organic
394 nitrides did contribute to the observed N K-edge spectra, although a targeted study on molecular
395 identification would be necessary to establish further certainty.

396 Oxygen K-edge spectra in Fig. 4C exhibited a large peak at 536.9 eV, which is a representative
 397 characteristic of sulfate-rich particles (Colberg et al., 2004; Slowik et al., 2011; Mikhailov et al., 2015;
 398 Pöhlker et al., 2014), consistent with the result of AMS. A smaller peak was observed at 532.5 eV,
 399 confirming the presence of ketone, aldehyde, or carboxyl functionalities (Moffet et al., 2011), which
 400 aligns with the results from C K-edge spectra. These compositions tend to take up water under humid
 401 conditions.

删除[Ruiqi Man]: Colberg et al., 2004; Slowik et al., 2011;
 Mikhailov et al., 2015; Pöhlker et al., 2014



402
 403 **Figure 4: NEXAFS spectra for individual particles at (A) carbon (C), (B) nitrogen (N), and (C) oxygen (O)**
 404 **K-edges. In panel (A), peaks were observed at 285.4, 286.7, and 288.6 eV, and two typical peaks appeared at**
 405 **around 296.8 and 299.6 eV in spectra (d) and (e). In panel (B), a main peak appeared at 405.7 eV, and a**
 406 **smaller peak appeared at 410.0 eV. In panel (C), a main peak appeared at 536.9 eV, and a smaller peak was**
 407 **at 532.5 eV. Each small case letter of a spectrum stands for the average result of all the pixels within an**
 408 **individual particle. The same letter in different panels doesn't refer to a same particle.**

409 4 Conclusions and implications

410 Particles in the atmosphere usually act as reaction vessels for heterogeneous reactive uptake of
 411 gaseous molecules, and heterogeneous processes play an important part in gas-particle partitioning and
 412 secondary aerosol formation (Abbatt et al., 2012; Davidovits et al., 2011; Kolb et al., 2010). However,
 413 determining the particle physicochemical properties is crucial but challenging due to the complexity
 414 and inhomogeneity of aerosols particles (Barbaray et al., 1979; Zong et al., 2022). So far, there is a lack
 415 of study on direct observation of the physicochemical properties of urban aerosols at the single particle
 416 level under different conditions, which hinders our understanding of the role of urban particle aerosols
 417 in multiphase and heterogeneous chemistry.

删除[Ruiqi Man]: which

418 In this study, we used STXM/NEXAFS spectroscopy combined with an environmental cell to
419 image and quantify the chemical morphology and water uptake behavior of individual submicron
420 particles collected in an urban pollution atmosphere. Results show that most organic compounds were
421 internally mixed with inorganic and/or soot, generally presenting a core-shell structure with an
422 inorganic core and an organic shell. Internally mixed particles composed of organic carbon and
423 inorganic matter dominated the particle population by $73.1 \pm 7.4\%$. At 86%RH, 41.6% of the particles
424 took up water, with OCIn particles making up 76.8% of these hygroscopic particles. The relatively low
425 hygroscopicity of bulk aerosols during the sampling period ($\kappa = 0.25 \pm 0.01$) helps to explain the
426 reason why only less than half of the particles took up water. Besides, the majority of particles still
427 showed a heterogeneous core-shell morphology under humid conditions.

428 This study directly displays the dominant chemical morphology (i.e., core-shell structure) and
429 hygroscopic behavior of individual submicron urban aerosol particles at the microscale. The uptake
430 coefficient onto aerosol particles with different phase states exhibit different patterns as the relative
431 humidity changes (Wang and Lu, 2016). For aqueous particles, the uptake coefficient is closely related
432 to RH (Wang and Lu, 2016). Specifically, when RH is lower than the DRH of the inorganic component,
433 the uptake coefficient increased with the increasing RH. When RH is higher than DRH, the uptake
434 coefficient remains constant. For solid particles, the relationship between the uptake coefficient and RH
435 usually depends on particle species (Wang and Lu, 2016). Results highlight the importance of taking
436 the core-shell structure into consideration for estimating the uptake coefficient and investigating
437 heterogeneous reactions at different humidities, which can improve our comprehension of atmospheric
438 processes of secondary aerosols in typical urban pollution atmospheres. ▾

439 Moreover, previous studies found that the reactive uptake coefficients of N_2O_5 on aqueous sulfuric
440 acid solutions coated with different kinds of organics vary (Cosman and Bertram, 2018; Cosman et al.,
441 2008). The reactive uptake coefficient decreased dramatically for straight-chain surfactants
442 (1-hexadecanol, 1-octadecanol, and stearic acid) by a factor of 17 - 61 depending on the surfactant type.
443 While, the presence of branched surfactant phytanic acid didn't show a obvious effect on the reactive
444 uptake coefficient compared to the uncoated solution. These results underlines that, the significant
445 impact of organic species on the reactive uptake coefficient. Therefore, on the basis of the high spectral
446 energy resolution of STXM/NEXAFS, it is instrumental to conduct research on the effect of organic
447 molecules and functional groups on heterogeneous reactions in future studies.

删除[Ruiqi Man]:

设置格式[Ruiqi Man]: 下标

设置格式[Ruiqi Man]: 下标

删除[Ruiqi Man]: previous studies found that

删除[Ruiqi Man]: organics

删除[Ruiqi Man]: mainly relies on organic species, organic content, and particle mixing state (Wagner et al., 2013)

删除[Ruiqi Man]: the basis of

删除[Ruiqi Man]: further

删除[Ruiqi Man]: study

448 **ASSOCIATED CONTENT**

449 ***Data availability.*** The data presented in this article can be accessed through the corresponding author
450 Zhijun Wu via E-mail (zhijunwu@pku.edu.cn).

451 ***Author contributions.*** YSZ, PAA, BBW, and JD measured the individual particle sample by
452 STXM/NEXAFS. YSZ, ZJW, YZ, YLG, QC, and SYC carried out the field observation and obtained
453 data. RQM and PAA processed and analyzed data. All authors discussed the results and contributed to
454 the writing of this paper. RQM prepared the manuscript. ZJW, PAA, JC, XRK, MA, and MH further
455 modified and improved the manuscript.

456 ***Competing Interests.*** The authors declare that they have no conflict of interest.

457 ***Acknowledgements.*** We gratefully acknowledge the Swiss Light Source (SLS) for providing a
458 platform for sample measurements. We also thank Benjamin Watts for helping us dealing with
459 technical problems about STXM/NEXAFS.

460 ***Financial support.*** This work has been supported by National Natural Science Foundation of China,
461 International (Regional) Cooperation and Communication Project (NSFC-STINT, China and Sweden;
462 grant No. 42011530121), NSFC (No. 41775133), and the SNSF Swiss Postdoctoral Fellowships (SPF,
463 grant TMPFP2_209830).

464 **References**

465 Abbatt, J. P. D., Lee, A. K. Y., and Thornton, J. A.: Quantifying trace gas uptake to tropospheric
466 aerosol: recent advances and remaining challenges, *Chem. Soc. Rev.*, 41, 6555–6581, DOI:
467 10.1039/c2cs35052a, 2012.

468 Alpert, P. A., Arroyo, P. C., Dou, J., Krieger, U. K., Steimer, S. S., Förster, J.-D., Ditas, F., Pöhlker, C.,
469 Rossignol, S., Passananti, M., Perrier, S., George, C., Shiraiwa, M., Berkemeier, T., Watts, B., and
470 Ammann, M.: Visualizing reaction and diffusion in xanthan gum aerosol particles exposed to
471 ozone, *Phys. Chem. Chem. Phys.*, 21, 20613–20627, DOI: 10.1039/c9cp03731d, 2019.

472 Alpert, P. A., Dou, J., Arroyo, P. C., Schneider, F., Xto, J., Luo, B. P., Peter, T., Huthwelker, T., Borca,
473 C. N., Henzler, K. D., Schaefer, T., Herrmann, H., Raabe, J., Watts, B., Krieger, U. K., and
474 Ammann, M.: Photolytic radical persistence due to anoxia in viscous aerosol particles, *Nat.*
475 *Commun.*, 12, 1769, DOI: 10.1038/s41467-021-21913-x, 2021.

476 Alpert, P. A., Kilthau, W. P., O'Brien, R. E., Moffet, R. C., Gilles, M. K., Wang, B. B., Laskin, A.,
477 Aller, J. Y., and Knopf, D. A.: Ice-nucleating agents in sea spray aerosol identified and quantified
478 with a holistic multimodal freezing model, *Sci. Adv.*, 8, eabq6842, DOI: 10.1126/sciadv.abq6842,
479 2022.

480 Barbaray, B., Contour, J. P., Mouvier, G., Barde, R., Maffiolo, G., and Millancourt, B.: Chemical
481 heterogeneity of aerosol samples as revealed by atomic absorption and x-ray photoelectron
482 spectroscopy, *Environ. Sci. Technol.*, 13, 1530–1532, DOI: 10.1021/es60160a008, 1979.

483 Bond, T. C., Habib, G., and Bergstrom, R. W.: Limitations in the enhancement of visible light
484 absorption due to mixing state, *J. Geophys. Res.: Atmos.*, 111, D20211, DOI:
485 10.1029/2006jd007315, 2006.

486 Bondy, A. L., Bonanno, D., Moffet, R. C., Wang, B. B., Laskin, A., and Ault, A. P.: The diverse
487 chemical mixing state of aerosol particles in the southeastern United States, *Atmos. Chem. Phys.*,
488 18, 12595–12612, DOI: 10.5194/acp-18-12595-2018, 2018.

489 Canagaratna, M. R., Jayne, J. T., Jimenez, J. L., Allan, J. D., Alfarra, M. R., Zhang, Q., Onasch, T. B.,
490 Drewnick, F., Coe, H., Middlebrook, A., Delia, A., Williams, L. R., Trimborn, A. M., Northway,
491 M. J., DeCarlo, P. F., Kolb, C. E., Davidovits, P., and Worsnop, D. R.: Chemical and
492 microphysical characterization of ambient aerosols with the aerodyne aerosol mass spectrometer,
493 *Mass Spectrom. Rev.*, 26, 185–222, DOI: 10.1002/mas.20115, 2007.

494 Chow, J. C., Watson, J. G., Mauderly, J. L., Costa, D.L., Wyzga, R.E., Vedral, S., Hidy, G. M.,
495 Altshuler, S. L., Marrack, D., Heuss, J. M., Wolff, G. T., Pope, C. A., and Dockery, D. W.: Health
496 effects of fine particulate air pollution: Lines that connect, *J. Air Waste Manage. Assoc.*, 56,
497 1368–1380, DOI: 10.1080/10473289.2006.10464545, 2006.

498 Colberg, C. A., Krieger, U. K., and Peter, T.: Morphological investigations of single levitated
499 $\text{H}_2\text{SO}_4/\text{NH}_3/\text{H}_2\text{O}$ aerosol particles during deliquescence/efflorescence experiments, *J. Phys. Chem.*
500 *A.*, 108, 2700–2709, DOI: 10.1021/jp037628r, 2004.

501 [Cosman, L. M., and Bertram, A. K.: Reactive Uptake of \$\text{N}_2\text{O}_5\$ on Aqueous \$\text{H}_2\text{SO}_4\$ Solutions Coated](#)
502 [with 1-Component and 2-Component Monolayers, J. Phys. Chem. A., 112, 4625–4635, DOI:](#)
503 [10.1021/jp8005469, 2008.](#)

504 [Cosman, L. M., Knopf, D. A., and Bertram, A. K.: \$\text{N}_2\text{O}_5\$ Reactive Uptake on Aqueous Sulfuric Acid](#)
505 [Solutions Coated with Branched and Straight-Chain Insoluble Organic Surfactants, J. Phys. Chem.](#)
506 [A., 112, 2386–2396, DOI: 10.1021/jp710685r, 2008.](#)

507 Davidovits, P., Kolb, C. E., Williams, L. R., Jayne, J. T., and Worsnop, D. R.: Update 1 of: Mass
508 Accommodation and Chemical Reactions at Gas-Liquid Interfaces, *Chem. Rev.*, 111,
509 PR76–PR109, DOI: 10.1021/cr100360b, 2011.

510 Davies, J. F. and Wilson, K. R.: Chapter 13 - Heterogeneous Reactions in Aerosol, *Physical Chemistry*
511 of Gas-Liquid Interfaces, edited by: Faust, J. A. and House, J. E., Elsevier, the Netherlands,
512 403–433, ISBN: 9780128136416, 2018.

513 Dou, X. D., Yu, S. C., Li, J. L., Sun, Y. H., Song, Z., Yao, N. N., and Li, P. F.: The WRF-CMAQ
514 Simulation of a Complex Pollution Episode with High-Level O_3 and $\text{PM}_{2.5}$ over the North China
515 Plain: Pollution Characteristics and Causes, *Atmosphere*, 15, 198, DOI: 10.3390/atmos15020198,
516 2024.

517 Ekimova, M., Quevedo, W., Szyc, L., Iannuzzi, M., Wernet, P., Odelius, M., and Nibbering, E. T. J.:
518 Aqueous Solvation of Ammonia and Ammonium: Probing Hydrogen Bond Motifs with FT-IR and
519 Soft X-ray Spectroscopy, *J. Am. Chem. Soc.*, 139, 12773–12783, DOI: 10.1021/jacs.7b07207,
520 2017.

521 Eom, H. J., Gupta, D., Li, X., Jung, H. J., Kim, H., and Ro, C. U.: Influence of collecting substrates on
522 the characterization of hygroscopic properties of inorganic aerosol particles, *Anal. Chem.*, 86,
523 2648–2656, DOI: 10.1021/ac4042075, 2014.

524 Fraund, M., Bonanno, D. J., China, S., Pham, D. Q., Veghte, D., Weis, J., Kulkarni, G., Teske, K.,
525 Gilles, M. K., Laskin, A., and Moffet, R. C.: Optical properties and composition of viscous
526 organic particles found in the Southern Great Plains, *Atmos. Chem. Phys.*, 20, 11593–11606, DOI:
527 10.5194/acp-20-11593-2020, 2020.

528 Freedman, M. A.: Phase separation in organic aerosol, *Chem. Soc. Rev.*, 46, 7694–7705, DOI:
529 10.1039/c6cs00783j, 2017.

530 Freedman, M. A.: Liquid-Liquid Phase Separation in Supermicrometer and Submicrometer Aerosol
531 Particles, *Acc. Chem. Res.*, 53, 1102–1110, DOI: 10.1021/acs.accounts.0c00093, 2020.

532 Fröhlich, R., Cubison, M. J., Slowik, J. G., Bukowiecki, N., Prévôt, A. S. H., Baltensperger, U.,
533 Schneider, J., Kimmel, J. R., Gonin, M., Rohner, U., Worsnop, D. R., and Jayne, J. T.: The
534 ToF-ACSM: a portable aerosol chemical speciation monitor with TOFMS detection, *Atmos. Meas.
535 Tech.*, 6, 3225–3241, [DOI: 10.5194/amt-6-3225-2013](#), 2013.

536 [Gao, J. J., Tian, H. Z., Cheng, K., Lu, L., Zheng, M., Wang, S. X., Hao, J. M., Wang, K., Hua, S. B.,
537 Zhu, C. Y., and Wang, Y.: The variation of chemical characteristics of PM_{2.5} and PM₁₀ and
538 formation causes during two haze pollution events in urban Beijing, China, *Atmos. Environ.*, 107,
539 1–8, DOI: 10.1016/j.atmosenv.2015.02.022, 2015.](#)

540 [Gao, J. J., Wang, K., Wang, Y., Liu, S. H., Zhu, C. Y., Hao, J. M., Liu, H. J., Hua, S. B., and Tian, H.
541 Z.: Temporal-spatial characteristics and source apportionment of PM_{2.5} as well as its associated
542 chemical species in the Beijing-Tianjin-Hebei region of China, *Environ. Pollut.*, 233, 714–724,
543 DOI: 10.1016/j.envpol.2017.10.123, 2018.](#)

544 [Gao, Y. and Anderson, J. R.: Characteristics of Chinese aerosols determined by individual-particle
545 analysis, *J. Geophys. Res.: Atmos.*, 106, 18037–18045, DOI: 10.1029/2000jd900725, 2001.](#)

546 George, C., Ammann, M., D'Anna, B., Donaldson, D. J., and Nizkorodov, S. A.: Heterogeneous
547 Photochemistry in the Atmosphere, *Chem. Rev.*, 115, 4218–4258, DOI: 10.1021/cr500648z, 2015.

548 George, I. J. and Abbatt, J. P. D.: Heterogeneous oxidation of atmospheric aerosol particles by
549 gas-phase radicalism, *Nat. Chem.*, 2, 713–722, DOI: 10.1038/nchem.806, 2010.

550 Ghorai, S. and Tivanski, A. V.: Hygroscopic Behavior of Individual Submicrometer Particles Studied
551 by X-ray Spectromicroscopy, *Anal. Chem.*, 82, 9289–9298, DOI: 10.1021/ac101797k, 2010.

552 [Guo, S., Hu, M., Zamora, M. L., Peng, J. F., Shang, D. J., Zheng, J., Du, Z. F., Wu, Z. J., Shao, M.,](#)
553 [Zeng, L. M., Molina, M. J., and Zhang, R. Y.: Elucidating severe urban haze formation in China,](#)
554 [Proc. Natl. Acad. Sci. U. S. A., 111, 17373–17378, DOI: 10.1073/pnas.1419604111, 2014.](#)

555 [Huang, R. J., Zhang, Y., Bozzetti, C., Ho, K. F., Cao, J. J., Han, Y., Daellenbach, K. R., Slowik, J. G.,](#)
556 [Platt, S. M., Canonaco, F., Zotter, P., Wolf, R., Pieber, S. M., Bruns, E. A., Crippa, M., Ciarelli,](#)
557 [G., Piazzalunga, A., Schwikowski, M., Abbaszade, G., Schnelle-Kreis, J., Zimmermann, R., An, Z.](#)
558 [S., Szidat, S., Baltensperger, U., ElHaddad, I., and Prévôt, A. S. H.: High secondary aerosol](#)
559 [contribution to particulate pollution during haze events in China, Nature, 514, 218–222, DOI:](#)
560 [10.1038/nature13774, 2014.](#)

561 Hopkins, R. J., Tivanski, A. V., Marten, B. D., and Gilles, M. K.: Chemical bonding and structure of
562 black carbon reference materials and individual carbonaceous atmospheric aerosols, J. Aerosol
563 Sci., 38, 573–591, DOI: 10.1016/j.jaerosci.2007.03.009, 2007.

564 Huthwelker, T., Zelenay, V., Birrer, M., Krepelova, A., Raabe, J., Tzvetkov, G., Vernooij, M. G. C.,
565 and Ammann, M.: An in situ cell to study phase transitions in individual aerosol particles on a
566 substrate using scanning transmission x-ray microspectroscopy, Rev. Sci. Instrum., 81, 113706,
567 DOI: 10.1063/1.3494604, 2010.

568 Jahl, L. G., Bowers, B. B., Jahn, L. G., Thornton, J. A., and Sullivan, R. C.: Response of the reaction
569 probability of N_2O_5 with authentic biomass-burning aerosol to high relative humidity, ACS Earth
570 Space Chem., 5, 2587–2598, DOI: 10.1021/acsearthspacechem.1c00227, 2021.

571 Jahn, L. G., Jahl, L. G., Bowers, B. B., and Sullivan, R. C.: Morphology of organic carbon coatings on
572 biomass-burning particles and their role in reactive gas uptake, ACS Earth Space Chem., 5,
573 2184–2195, DOI: 10.1021/acsearthspacechem.1c00237, 2021.

574 Knopf, D. A., Wang, P. W., Wong, B. Y., Tomlin, J. M., Veghte, D. P., Lata, N. N., China, S., Laskin,
575 A., Moffet, R. C., Aller, J. Y., Marcus, M. A., and Wang, J.: Physicochemical characterization of
576 free troposphere and marine boundary layer ice-nucleating particles collected by aircraft in the
577 eastern North Atlantic, Atmos. Chem. Phys., 23, 8659–8681, DOI: 10.5194/acp-23-8659-2023,
578 2023.

579 Kolb, C. E., Cox, R. A., Abbatt, J. P. D., Ammann, M., Davis, E. J., Donaldson, D. J., Garrett, B. C.,
580 George, C., Griffiths, P. T., Hanson, D. R., Kulmala, M., McFiggans, G., Pöschl, U., Riipinen, I.,
581 Rossi, M. J., Rudich, Y., Wagner, P. E., Winkler, P. M., Worsnop, D. R., and O'Dowd, C. D.: An

582 overview of current issues in the uptake of atmospheric trace gases by aerosols and clouds, *Atmos.*
583 *Chem. Phys.*, 10, 10561–10605, DOI: 10.5194/acp-10-10561-2010, 2010.

584 Krieger, U. K., Marcolli, C., and Reid, J. P.: Exploring the complexity of aerosol particle properties
585 and processes using single particle techniques, *Chem. Soc. Rev.*, 41, 6631–6662, DOI:
586 10.1039/c2cs35082c, 2012.

587 Lata, N. N., Zhang, B., Schum, S., Mazzoleni, L., Brimberry, R., Marcus, M. A., Cantrell, W. H.,
588 Fialho, P., Mazzoleni, C., and China, S.: Aerosol Composition, Mixing State, and Phase State of
589 Free Tropospheric Particles and Their Role in Ice Cloud Formation, *ACS Earth Space Chem.*, 5,
590 3499–3510, DOI: 10.1021/acsearthspacechem.1c00315, 2021.

591 Latham, K. G., Simone, M. I., Dose, W. M., Allen, J. A., and Donne, S. W.: Synchrotron based
592 NEXAFS study on nitrogen doped hydrothermal carbon: Insights into surface functionalities and
593 formation mechanisms, *Carbon*, 114, 566–578, DOI: 10.1016/j.carbon.2016.12.057, 2017.

594 [Lei, L., Zhou, W., Chen, C., He, Y., Li, Z. J., Sun, J. X., Tang, X., Fu, P. Q., Wang, Z. F., and Sun, Y.](#)
595 [L.: Long-term characterization of aerosol chemistry in cold season from 2013 to 2020 in Beijing,](#)
596 [China, Environ. Pollut., 268, 115952, DOI: 10.1016/j.envpol.2020.115952, 2021.](#)

597 Leinweber, P., Kruse, J., Walley, F. L., Gillespie, A., Eckhardt, K. U., Blyth, R. I. R., and Regier, T.:
598 Nitrogen K-edge XANES - An overview of reference compounds used to identify 'unknown'
599 organic nitrogen in environmental samples, *J. Synchrotron Radiat.*, 14, 500–511, DOI:
600 10.1107/s0909049507042513, 2007.

601 Li, W. J., Shao, L. Y., Zhang, D. Z., Ro, C. U., Hu, M., Bi, X. H., Geng, H., Matsuki, A., Niu, H. Y.,
602 and Chen, J. M.: A review of single aerosol particle studies in the atmosphere of East Asia:
603 morphology, mixing state, source, and heterogeneous reactions, *J. Cleaner Prod.*, 112, 1330–1349,
604 DOI: 10.1016/j.jclepro.2015.04.050, 2016.

605 Li, W. J., Liu, L., Zhang, J., Xu, L., Wang, Y. Y., Sun, Y. L., and Shi, Z. B.: Microscopic Evidence for
606 Phase Separation of Organic Species and Inorganic Salts in Fine Ambient Aerosol Particles,
607 *Environ. Sci. Technol.*, 55, 2234–2242, DOI: 10.1021/acs.est.0c02333, 2021.

608 [Li, Y. J., Sun, Y. L., Zhang, Q., Li, X., Li, M., Zhou, Z., and Chan, C. K.: Real-time chemical](#)
609 [characterization of atmospheric particulate matter in China: A review, Atmos. Environ., 158,](#)
610 [270–304, DOI: 10.1016/j.atmosenv.2017.02.027, 2017.](#)

611 [Liu, Z. R., Gao, W. K., Yu, Y. C., Hu, B., Xin, J. Y., Sun, Y., Wang, L. L., Wang, G. H., Bi, X. H.,](#)
612 [Zhang, G. H., Xu, H. H., Cong, Z. Y., He, J., Xu, J. S., and Wang, Y. S.: Characteristics of PM_{2.5}](#)
613 [mass concentrations and chemical species in urban and background areas of China: emerging](#)
614 [results from the CARE-China network, Atmos. Chem. Phys., 18, 8849–8871, DOI:](#)
615 [10.5194/acp-18-8849-2018, 2018.](#)

616 Martin, S. T.: Phase transitions of aqueous atmospheric particles, *Chem. Rev.*, 100, 3403–3453, DOI:
617 10.1021/cr990034t, 2001.

618 McCormick, R. A. and Ludwig, J. H.: Climate Modification by Atmospheric Aerosols, *Science*, 156,
619 1358–1359, DOI: 10.1126/science.156.3780.1358, 1967.

620 Middlebrook, A. M., Bahreini, R., Jimenez, J. L., and Canagaratna, M. R.: Evaluation of
621 Composition-Dependent Collection Efficiencies for the Aerodyne Aerosol Mass Spectrometer
622 using Field Data, *Aerosol Sci. Technol.*, 46, 258–271, [DOI: 10.1080/02786826.2011.620041](#),
623 2012.

624 Mikhailov, E. F., Mironov, G. N., Pöhlker, C., Chi, X., Krüger, M. L., Shiraiwa, M., Förster, J. D.,
625 Pöschl, U., Vlasenko, S. S., Ryshkevich, T. I., Weigand, M., Kilcoyne, A. L. D., and Andreae, M.
626 O.: Chemical composition, microstructure, and hygroscopic properties of aerosol particles at the
627 Zotino Tall Tower Observatory (ZOTTO), Siberia, during a summer campaign, *Atmos. Chem.*
628 *Phys.*, 15, 8847–8869, DOI: 10.5194/acp-15-8847-2015, 2015.

629 Moffet, R. C., Henn, T., Laskin, A., and Gilles, M. K.: Automated Chemical Analysis of Internally
630 Mixed Aerosol Particles Using X-ray Spectromicroscopy at the Carbon K-Edge, *Anal. Chem.*, 82,
631 7906–7914, DOI: 10.1021/ac1012909, 2010a.

632 Moffet, R. C., Henn, T. R., Tivanski, A. V., Hopkins, R. J., Desyaterik, Y., Kilcoyne, A. L. D.,
633 Tyliszczak, T., Fast, J., Barnard, J., Shuthanandan, V., Cliff, S. S., Perry, K. D., Laskin, A., and
634 Gilles, M. K.: Microscopic characterization of carbonaceous aerosol particle aging in the outflow
635 from Mexico City, *Atmos. Chem. Phys.*, 10, 961–976, DOI: 10.5194/acp-10-961-2010, 2010b.

636 Moffet, R. C., Tivanski A. V., and Gilles M. K.: Scanning Transmission X-ray Microscopy
637 Applications in Atmospheric Aerosol Research, *Fundamentals and Applications in Aerosol*
638 *Spectroscopy*, edited by: Signorell, R., and Reid, J. P., CRC Press, the U.S., 419–462, ISBN:
639 9781420085617, 2011.

640 Moffet, R. C., Rödel, T. C., Kelly, S. T., Yu, X. Y., Carroll, G. T., Fast, J., Zaveri, R. A., Laskin, A.,
641 and Gilles, M. K.: Spectro-microscopic measurements of carbonaceous aerosol aging in Central
642 California, *Atmos. Chem. Phys.*, 13, 10445–10459, DOI: 10.5194/acp-13-10445-2013, 2013.

643 Moffet, R. C., O'Brien, R. E., Alpert, P. A., Kelly, S. T., Pham, D. Q., Gilles, M. K., Knopf, D. A., and
644 Laskin, A.: Morphology and mixing of black carbon particles collected in central California
645 during the CARES field study, *Atmos. Chem. Phys.*, 16, 14515–14525, DOI:
646 10.5194/acp-16-14515-2016, 2016.

647 Noll, K. E., Mueller, P. K., and Imada, M.: Visibility and aerosol concentration in urban air, *Atmos.*
648 *Environ.*, 2, 465–475, DOI: 10.1016/0004-6981(68)90040-1, 1968.

649 O'Brien, R. E., Wang, B. B., Kelly, S. T., Lundt, N., You, Y., Bertram, A. K., Leone, S. R., Laskin, A.,
650 and Gilles, M. K.: Liquid-Liquid Phase Separation in Aerosol Particles: Imaging at the Nanometer
651 Scale, *Environ. Sci. Technol.*, 49, 4995–5002, DOI: 10.1021/acs.est.5b00062, 2015.

652 Peng, C., Chen, L. X. D., and Tang, M. J.: A database for deliquescence and efflorescence relative
653 humidities of compounds with atmospheric relevance, *Fundam. Res.*, 2, 578–587, DOI:
654 10.1016/j.fmre.2021.11.021, 2022.

655 Penner, J. E. and Novakov, T.: Carbonaceous particles in the atmosphere: A historical perspective to
656 the Fifth International Conference on Carbonaceous Particles in the Atmosphere, *J. Geophys. Res.:*
657 *Atmos.*, 101, 19373–19378, DOI: 10.1029/96JD01175, 1996.

658 [Petters, M. D. and Kreidenweis, S. M.: A single parameter representation of hygroscopic growth and](#)
659 [cloud condensation nucleus activity, *Atmos. Chem. Phys.*, 7, 1961–1971, DOI:](#)
660 [10.5194/acp-7-1961-2007, 2007.](#)

661 Piens, D. S., Kelly, S. T., Harder, T. H., Petters, M. D., O'Brien, R. E., Wang, B. B., Teske, K., Dowell,
662 P., Laskin, A., and Gilles, M. K.: Measuring Mass-Based Hygroscopicity of Atmospheric Particles
663 through in Situ Imaging, *Environ. Sci. Technol.*, 50, 5172–5180, DOI: 10.1021/acs.est.6b00793,
664 2016.

665 Pöhlker, C., Saturno, J., Krüger, M. L., Förster, J. D., Weigand, M., Wiedemann, K. T., Bechtel, M.,
666 Artaxo, P., and Andreae, M. O.: Efflorescence upon humidification? X-ray microspectroscopic in
667 situ observation of changes in aerosol microstructure and phase state upon hydration, *Geophys.*
668 *Res. Lett.*, 41, 3681–3689, DOI: 10.1002/2014gl059409, 2014.

删除[Ruiqi Man]: .

669 Prather, K. A., Bertram, T. H., Grassian, V. H., Deane, G. B., Stokes, M. D., DeMott, P. J., Aluwihare,
670 L. I., Palenik, B. P., Azam, F., Seinfeld, J. H., Moffet, R. C., Molina, M. J., Cappa, C. D., Geiger,
671 F. M., Roberts, G. C., Russell, L. M., Ault, A. P., Baltrusaitis, J., Collins, D. B., Corrigan, C. E.,
672 Cuadra-Rodriguez, L. A., Ebbin, C. J., Forestieri, S. D., Guasco, T. L., Hersey, S. P., Kim, M. J.,
673 Lambert, W. F., Modini, R. L., Mui, W., Pedler, B. E., Ruppel, M. J., Ryder, O. S., Schoepp, N.
674 G., Sullivan, R. C., and Zhao, D. F.: Bringing the ocean into the laboratory to probe the chemical
675 complexity of sea spray aerosol, Proc. Natl. Acad. Sci. U. S. A., 110, 7550–7555, DOI:
676 10.1073/pnas.1300262110, 2013.

677 Raabe, J., Tzvetkov, G., Flechsig, U., Böge, M., Jaggi, A., Sarafimov, B., Vernooij, M. G. C.,
678 Huthwelker, T., Ade, H., Kilcoyne, D., Tyliszczak, T., Fink, R. H., and Quitmann, C.: PolLux: A
679 new facility for soft x-ray spectromicroscopy at the Swiss Light Source, Rev. Sci. Instrum., 79,
680 113704, DOI: 10.1063/1.3021472, 2008.

681 Rasool, S. I. and Schneider, S. H.: Atmospheric Carbon Dioxide and Aerosols: Effects of Large
682 Increases on Global Climate, Science, 173, 138–141, DOI: 10.1126/science.173.3992.138, 1971.

683 Reynolds, R. S. and Wilson, K. R.: Unraveling the Meaning of Effective Uptake Coefficients in
684 Multiphase and Aerosol Chemistry, Acc. Chem. Res., 58, 366–374, [DOI](#):
685 10.1021/acs.accounts.4c00662, 2025.

686 Riemer, N., Ault, A. P., West, M., Craig, R. L., and Curtis, J. H.: Aerosol Mixing State: Measurements,
687 Modeling, and Impacts, Rev. Geophys., 57, 187–249, DOI: 10.1029/2018rg000615, 2019.

688 Shao, L. Y., Liu, P. J., Jones, T., Yang, S. S., Wang, W. H., Zhang, D. Z., Li, Y. W., Yang, C.-X., Xing,
689 J. P., Hou, C., Zhang, M. Y., Feng, X. L., Li, W. J., and BéruBé K.: A review of atmospheric
690 individual particle analyses: Methodologies and applications in environmental research,
691 Gondwana Res., 110, 347–369, DOI: 10.1016/j.gr.2022.01.007, 2022.

692 [Shen, X. J., Sun, J. Y., Zhang, X. Y., Zhang, Y. M., Zhong, J. T., Wang, X., Wang, Y. Q., and Xia, C.:](#)
693 [Variations in submicron aerosol liquid water content and the contribution of chemical components](#)
694 [during heavy aerosol pollution episodes in winter in Beijing, Sci. Total Environ., 693, 133521,](#)
695 [DOI: 10.1016/j.scitotenv.2019.07.327, 2019.](#)

696 Slowik, J. G., Cziczo, D. J., and Abbatt, J. P. D.: Analysis of cloud condensation nuclei composition
697 and growth kinetics using a pumped counterflow virtual impactor and aerosol mass spectrometer,
698 Atmos. Meas. Tech., 4, 1677–1688, DOI: 10.5194/amt-4-1677-2011, 2011.

699 Smith, J. W., Lam, R. K., Shih, O., Rizzuto, A. M., Prendergast, D., and Saykally, R. J.: Properties of
700 aqueous nitrate and nitrite from x-ray absorption spectroscopy, *J. Chem. Phys.*, 143, 084503, DOI:
701 10.1063/1.4928867, 2015.

702 [Song, M., Jeong, R., Kim, D., Qiu, Y. T., Meng, X. X. Y., Wu, Z. J., Zuend, A., Ha, Y., Kim, C., Kim, H., Gaikwad, S., Jang, K. S., Lee, J. Y., and Ahn, J.: Comparison of Phase States of PM_{2.5} over Megacities, Seoul and Beijing, and Their Implications on Particle Size Distribution, Environ. Sci. Technol., 56, 17581–17590, DOI: 10.1021/acs.est.2c06377, 2022.](#)

703

704

705

706 Stokes, R. H. and Robinson, R. A.: Interactions in aqueous nonelectrolyte solutions. I. Solute-solvent
707 equilibria, *J. Phys. Chem.*, 70, 2126–2131, DOI: 10.1021/j100879a010, 1966.

708 Su, H., Cheng, Y. F., and Pöschl, U.: New Multiphase Chemical Processes Influencing Atmospheric
709 Aerosols, Air Quality, and Climate in the Anthropocene, *Acc. Chem. Res.*, 53, 2034–2043, DOI:
710 10.1021/acs.accounts.0c00246, 2020.

711 [Sun, Y. L., Wang, Z. F., Fu, P. Q., Yang, T., Jiang, Q., Dong, H. B., Li, J., and Jia, J. J.: Aerosol composition, sources and processes during wintertime in Beijing, China, *Atmos. Chem. Phys.*, 13, 4577–4592, DOI: 10.5194/acp-13-4577-2013, 2013.](#)

712

713

714 Tang, L. Z., Shang, D. J., Fang, X., Wu, Z. J., Qiu, Y. T., Chen, S. Y., Li, X., Zeng, L. M., Guo, S., and
715 Hu, M.: More Significant Impacts From New Particle Formation on Haze Formation During
716 COVID-19 Lockdown, *Geophys. Res. Lett.*, 48, e2020GL091591, DOI: 10.1029/2020gl091591,
717 2021.

718 Tang, M. J., Cziczo, D. J., and Grassian, V. H.: Interactions of Water with Mineral Dust Aerosol:
719 Water Adsorption, Hygroscopicity, Cloud Condensation, and Ice Nucleation, *Chem. Rev.*, 116,
720 4205–4259, DOI: 10.1021/acs.chemrev.5b00529, 2016.

721 Tang, M. J., Chan, C. K., Li, Y. J., Su, H., Ma, Q. X., Wu, Z. J., Zhang, G. H., Wang, Z., Ge, M. F., Hu,
722 M., He, H., and Wang, X. M.: A review of experimental techniques for aerosol hygroscopicity
723 studies, *Atmos. Chem. Phys.*, 19, 12631–12686, DOI: 10.5194/acp-19-12631-2019, 2019.

724 Tomlin, J. M., Weis, J., Veghte, D. P., China, S., Fraund, M., He, Q., Reicher, N., Li, C., Jankowski, K.
725 A., Rivera-Adorno, F. A., Morales, A. C., Rudich, Y., Moffet, R. C., Gilles, M. K., and Laskin, A.:
726 Chemical composition and morphological analysis of atmospheric particles from an intensive
727 bonfire burning festival, *Environ. Sci.: Atmos.*, 2, 616–633, DOI: 10.1039/d2ea00037g, 2022.

728 Ulbrich, I. M., Canagaratna, M. R., Zhang, Q., Worsnop, D. R., and Jimenez, J. L.: Interpretation of
729 organic components from Positive Matrix Factorization of aerosol mass spectrometric data, *Atmos.*
730 *Chem. Phys.*, 9, 2891–2918, DOI: 10.5194/acp-9-2891-2009, 2009.

731 Wagner, N. L., Riedel, T. P., Young, C. J., Bahreini, R., Brock, C. A., Dubé, W. P., Kim, S.,
732 Middlebrook, A. M., Öztürk, F., Roberts, J. M., Russo, R., Sive, B., Swarthout, R., Thornton, J. A.,
733 VandenBoer, T. C., Zhou, Y., and Brown, S. S.: N₂O₅ uptake coefficients and nocturnal NO₂
734 removal rates determined from ambient wintertime measurements, *J. Geophys. Res.: Atmos.*, 118,
735 9331–9350, DOI: 10.1002/jgrd.50653, 2013.

736 [Wang, H. C., and Lu, K. D.: Determination and Parameterization of the Heterogeneous Uptake](#)
737 [Coefficient of Dinitrogen Pentoxide \(N₂O₅\), *Prog. Chem.*, 28, 917–933, DOI: 10.7536/PC151225,](#)
738 [2016.](#)

设置格式[Ruiqi Man]: 下标

设置格式[Ruiqi Man]: 下标

739 [Wang, Y. C., Chen, J., Wang, Q. Y., Qin, Q. D., Ye, J. H., Han, Y. M., Li, L., Zhen, W., Zhi, Q., Zhang,](#)
740 [Y. X., and Cao, J. J.: Increased secondary aerosol contribution and possible processing on polluted](#)
741 [winter days in China, *Environ. Int.*, 127, 78–84, DOI: 10.1016/j.envint.2019.03.021, 2019.](#)

742 [Wang, Y. S., Yao, L., Wang, L. L., Liu, Z. R., Ji, D. S., Tang, G. Q., Zhang, J. K., Sun, Y., Hu, B., and](#)
743 [Xin, J. Y.: Mechanism for the formation of the January 2013 heavy haze pollution episode over](#)
744 [central and eastern China, *Sci. China: Earth Sci.*, 57, 14–25, DOI: 10.1007/s11430-013-4773-4,](#)
745 [2014.](#)

746 Warwick, T., Franck, K., Kortright, J. B., Meigs, G., Moronne, M., Myneni, S., Rotenberg, E., Seal, S.,
747 Steele, W. F., Ade, H., Garcia, A., Cerasari, S., Delinger, J., Hayakawa, S., Hitchcock, A. P.,
748 Tyliszczak, T., Kikuma, J., Rightor, E. G., Shin, H. J., and Tonner, B. P.: A scanning transmission
749 x-ray microscope for materials science spectromicroscopy at the advanced light source, *Rev. Sci.*
750 *Instrum.*, 69, 2964–2973, DOI: 10.1063/1.1149041, 1998.

751 Wu, L. and Ro, C. U.: Aerosol Hygroscopicity on A Single Particle Level Using Microscopic and
752 Spectroscopic Techniques: A Review, *Asian J. Atmos. Environ.*, 14, 177–209, DOI:
753 10.5572/ajae.2020.14.3.177, 2020.

754 Wu, Z. J., Hu, M., Liu, S., Wehner, B., Bauer, S., Ma ßling, A., Wiedensohler, A., Petäjä, T., Dal Maso,
755 M., and Kulmala, M.: New particle formation in Beijing, China: Statistical analysis of a 1-year
756 data set, *J. Geophys. Res.: Atmos.*, 112, D0920, DOI: 10.1029/2006jd007406, 2007.

757 Wu, Z. J., Zheng, J., Shang, D. J., Du, Z. F., Wu, Y. S., Zeng, L. M., Wiedensohler, A., and Hu, M.:
758 Particle hygroscopicity and its link to chemical composition in the urban atmosphere of Beijing,
759 China, during summertime, *Atmos. Chem. Phys.*, 16, 1123–1138, DOI:
760 10.5194/acp-16-1123-2016, 2016.

761 Wu, Z. J., Zheng, J., Wang, Y., Shang, D. J., Du, Z. F., Zhang, Y. H., and Hu, M.: Chemical and
762 physical properties of biomass burning aerosols and their CCN activity: A case study in Beijing,
763 China, *Sci. Total Environ.*, 579, 1260–1268, DOI: 10.1016/j.scitotenv.2016.11.112, 2017.

764 Xiao, Z. M., Xu, H., Gao, J. Y., Cai, Z. Y., Bi, W. K., Li, P., Yang, N., Deng, X. W., Ji, Y. F.:
765 Characteristics and Sources of PM_{2.5}-O₃ Compound Pollution in Tianjin, *Environmental Science*
766 (Chinese), 43, 1140–1150, DOI: 10.13227/j.hjkx.202108164, 2022.

767 You, Y., Renbaum-Wolff, L., Carreras-Sospedra, M., Hanna, S. J., Hiranuma, N., Kamal, S., Smith, M.
768 L., Zhang, X. L., Weber, R. J., Shilling, J. E., Dabdub, D., Martin, S. T., and Bertram, A. K.:
769 Images reveal that atmospheric particles can undergo liquid-liquid phase separations, *Proc. Natl.*
770 *Acad. Sci. U. S. A.*, 109, 13188–13193, DOI: 10.1073/pnas.1206414109, 2012.

771 You, Y., Renbaum-Wolff, L., and Bertram, A. K.: Liquid-liquid phase separation in particles
772 containing organics mixed with ammonium sulfate, ammonium bisulfate, ammonium nitrate or
773 sodium chloride, *Atmos. Chem. Phys.*, 13, 11723–11734, DOI: 10.5194/acp-13-11723-2013,
774 2013.

775 You, Y., Smith, M. L., Song, M. J., Martin, S. T., and Bertram, A. K.: Liquid–liquid phase separation
776 in atmospherically relevant particles consisting of organic species and inorganic salts, *Int. Rev.*
777 *Phys. Chem.*, 33, 43–77, DOI: 10.1080/0144235x.2014.890786, 2014.

778 Yu, X., Li, Q. F., Liao, K. Z., Li, Y. M., Wang, X. M., Zhou, Y., Liang, Y. M., and Yu, J. Z.: New
779 measurements reveal a large contribution of nitrogenous molecules to ambient organic aerosol, *npj*
780 *Clim. Atmos. Sci.*, 7, 72, DOI: 10.1038/s41612-024-00620-6, 2024.

781 Zelenay, V., Ammann, M., Křepelová, A., Birrer, M., Tzvetkov, G., Vernooy, M. G. C., Raabe, J., and
782 Huthwelker, T.: Direct observation of water uptake and release in individual submicrometer sized
783 ammonium sulfate and ammonium sulfate/adipic acid particles using X-ray microspectroscopy, *J.*
784 *Aerosol Sci.*, 42, 38–51, DOI: 10.1016/j.jaerosci.2010.11.001, 2011a.

785 Zelenay, V., Huthwelker, T., Krepelová, A., Rudich, Y., and Ammann, M.: Humidity driven nanoscale
786 chemical separation in complex organic matter, *Environ. Chem.*, 8, 450–460, DOI:
787 10.1071/en11047, 2011b.

788 Zhang, J., Wang, Y. Y., Teng, X. M., Liu, L., Xu, Y. S., Ren, L. H., Shi, Z. B., Zhang, Y., Jiang, J. K.,
789 Liu, D. T., Hu, M., Shao, L. Y., Chen, J. M., Martin, S. T., Zhang, X. Y., and Li, W. J.:
790 Liquid-liquid phase separation reduces radiative absorption by aged black carbon aerosols,
791 *Commun. Earth Environ.*, 3, 128, DOI: 10.1038/s43247-022-00462-1, 2022.

792 [Zhao, X. J., Zhao, P. S., Xu, J., Meng, W., Pu, W. W., Dong, F., He, D., and Shi, Q. F.: Analysis of a](#)
793 [winter regional haze event and its formation mechanism in the North China Plain, *Atmos. Chem.*](#)
794 [*Phys.*, 13, 5685–5696, DOI: 10.5194/acp-13-5685-2013, 2013.](#)

795 Zheng, Y., Cheng, X., Liao, K. R., Li, Y. W., Li, Y. J., Huang, R.-J., Hu, W. W., Liu, Y., Zhu, T., Chen,
796 S. Y., Zeng, L. M., Worsnop, D. R., and Chen, Q.: Characterization of anthropogenic organic
797 aerosols by TOF-ACSM with the new capture vaporizer, *Atmos. Meas. Tech.*, 13, 2457–2472,
798 DOI: 10.5194/amt-13-2457-2020, 2020.

799 Zheng, Y., Miao, R. Q., Zhang, Q., Li, Y. W., Cheng, X., Liao, K. R., Koenig, T. K., Ge, Y. L., Tang,
800 L. Z., Shang, D. J., Hu, M., Chen, S. Y., and Chen, Q.: Secondary Formation of Submicron and
801 Supermicron Organic and Inorganic Aerosols in a Highly Polluted Urban Area, *J. Geophys. Res.: Atmos.*, 128, e2022JD037865, DOI: 10.1029/2022jd037865, 2023.

803 Ziemann, P. J. and Atkinson, R.: Kinetics, products, and mechanisms of secondary organic aerosol
804 formation, *Chem. Soc. Rev.*, 41, 6582–6605, DOI: 10.1039/c2cs35122f, 2012.

805 Zong, T. M., Wang, H. C., Wu, Z. J., Lu, K. D., Wang, Y., Zhu, Y. S., Shang, D. J., Fang, X., Huang,
806 X. F., He, L. Y., Ma, N., Gröss, J., Huang, S., Guo, S., Zeng, L. M., Herrmann, H., Wiedensohler,
807 A., Zhang, Y. H., and Hu, M.: Particle hygroscopicity inhomogeneity and its impact on reactive
808 uptake, *Sci. Total Environ.*, 811, 151364, DOI: 10.1016/j.scitotenv.2021.151364, 2022.